Analysis of K_α Line Emission from Aluminum Plasmas Created by Intense Proton Beams

J.J. MacFarlane, P. Wang, J. Bailey,
T.A. Mehlhorn, R.J. Dukart, R.C. Mancini

September 1992

UWFDM-906

Phys. Rev. E (1993).

FUSION TECHNOLOGY INSTITUTE

UNIVERSITY OF WISCONSIN

MADISON WISCONSIN

Analysis of K_α Line Emission from Aluminum Plasmas Created by Intense Proton Beams

J. J. MacFarlane and P. Wang

Fusion Technology Institute, University of Wisconsin, Madison, WI 53706

J. Bailey, T. A. Mehlhorn, and R. J. Dukart

Sandia National Laboratories, Albuquerque, NM 87185

R. C. Mancini

Department of Physics, University of Florida, Gainesville, FL 32611

Revised November 1992

PACS Numbers: 52.70.L, 52.25.J, 32.80.H, 32.70

Abstract

X-ray satellite line emission from targets irradiated by intense light ion beams can be used to diagnose plasma conditions and beam properties. We present results from our analysis of the first spectroscopic measurements of x-ray K_α satellites emitted from a target irradiated by an intense light ion beam. In this experiment an Al target was irradiated with a 4-6 MeV proton beam with a peak power density of 1-2 TW/cm^2. Up to 15 percent of the beam electrical current was in the form of carbon contaminants. A time-integrated spectrum was obtained with a resolution of $\lambda/\Delta\lambda > 1200$. Collisional radiative equilibrium (CRE) calculations were performed to study the dependence of the Al K_α emission spectrum on plasma and beam properties. Radiative and beam-induced transitions were included in the statistical equilibrium model. Atomic data for the CRE calculations were computed using a combination of Hartree-Fock, plane wave Born approximation, and semiclassical impact parameter models. Predictions for the time-dependent plasma conditions during the experiment were obtained from radiation-hydrodynamic simulations. Detailed Stark line broadening calculations were performed to study the physical processes affecting line profiles. We also consider the effects of opacity and the contribution from K_α transitions involving excited states. Our results suggest that emission spectroscopy of x-ray satellite lines can be a valuable technique for determining plasma conditions in intense light ion beam experiments.

I. Introduction

Spectroscopic observation of x-ray lines resulting from inner-shell transitions can be used to diagnose plasma conditions in targets irradiated by intense laser or ion beams. Absorption spectroscopy of K- and L-shell lines [1-7] has recently been used to diagnose plasma temperatures and densities in laser-produced plasmas and to measure opacities. For plasmas created by intense ion beams, emission spectroscopy can be used [8,9] because beam-induced ionizations produce K-shell vacancies which are subsequently filled during resonance fluorescence and autoionizing transitions. Thus, in addition to heating the target material the ion beam produces x-ray emission lines, thereby negating the need for a backlighter.

First spectroscopic observation of x-ray satellite lines in an intense proton beam experiment was recently made during a Particle Beam Fusion Accelerator II (PBFA-II) experiment at Sandia National Laboratories [8]. In this experiment an aluminum target was irradiated with a 4-6 MeV, 1-2 TW/cm^2 proton beam. An elliptic crystal spectrograph was used to obtain a time-integrated spectrum. Proton impact ionization of K-shell electrons populates autoionizing states, which then produce fluorescence line emission during K_α ($2p \rightarrow 1s$) transitions. Because of changes in electron screening effects, the K_α lines from Ne-like to He-like Al exhibit small, but detectable shifts to shorter wavelengths. The complete spectrum thus consists of neutral-atom K_α lines plus a series of blue-shifted satellites. K_α line spectra can therefore provide a measure of the ionization distribution in a plasma, and from that, constraints on plasma conditions.

The purpose of this investigation has been twofold: (1) to develop a good understanding of the physical processes that affect the K_α spectrum from targets heated by intense ion beams, and (2) to investigate the plasma conditions attained during the experiment reported in Ref. 8. In regards to the first item, we have studied several processes in detail. First, we have examined the contributions from excited states (i.e.,

states which were thermally excited prior to proton impact) to K_α emission spectra. Second, we have studied the relationship between temperature, ionization distribution, and K_α spectrum, and the effect line opacity has on skewing the resulting spectrum toward apparent higher ionization state. And third, in a separate set of calculations the sensitivity of K_α satellite line profiles to temperature and density was examined.

In regards to our second goal, two features about the target complicated our analysis: opacity and geometry. Part of this stems from the fact that the primary objective of the experiment reported in Ref. 8 was not to diagnose plasma temperatures. The thickness of the Al target (75 μm) was dictated by the stopping range of 5 MeV protons. At this thickness optical depths for both the x-ray continuum and K_α lines exceed unity. Additional complexity is introduced by the experiment geometry: the ions are accelerated from a barrel-shaped diode and irradiate a conical target. The shape of the expanding target plasma can only be calculated approximately with 1-D simulation codes. Despite these obstacles, we have been able to estimate the maximum plasma temperature attained in the *observable* part of the plasma, to qualitatively address the question of where the K_α photons seen by the detector originate, and the role of target heating by carbon ions in the beam. In addition, this study lays the groundwork for diagnosing plasma conditions in future experiments.

In our theoretical analysis, we have performed collisional-radiative equilibrium (CRE), atomic physics, line broadening, and hydrodynamic modelling calculations. Single-configuration and multiconfiguration Hartree-Fock calculations were performed to identify lines in the observed spectrum. Level populations and spectra were computed using a CRE code which models the effects of proton-impact ionization and radiation-induced transitions on the atomic level populations in addition to the usual collisional and radiative processes occuring in any hot laboratory plasma. The effects of opacity and the contribution of excited states have been examined in detail. To study the

sensitivity of line profiles to the plasma conditions, Stark line broadening calculations were performed for several of the F-like and O-like Al lines using a code which includes broadening effects due to both electrons and ions. Radiation-hydrodynamic simulations were performed in conjunction with particle-in-cell (PIC) calculations to predict the time-dependent evolution of the target plasma conditions and to assess the potential for target heating by contaminant carbon ions in the beam.

The outline of this paper is as follows. In Section II we summarize the experimental setup and spectroscopic measurements. An overview of our theoretical models is presented in Section III. In Section IV we discuss in detail physical processes which affect the K_α spectrum. In Section V we present results from hydrodynamic simulations of the PBFA-II experiment and a series of CRE calculations based on hydrodynamic predictions. We compare calculated and experimental spectra, and discuss the ramifications of our results for determining experimental plasma conditions. A summary of this investigation is presented in Section VI.

II. Experimental Setup and Measurements

An experiment to assess the potential for using K_α satellite emission as a plasma diagnostic has recently been performed with an intense proton beam generated by PBFA-II [8,10,11]. The accelerator electrical power pulse is converted into an ion beam using the applied-B diode [12] shown schematically in Fig. 1. This configuration is known as a "barrel" diode because ions accelerate radially inward from the azimuthally symmetric anode (the "barrel") toward a target at the center. Present target experiments use a proton beam generated with this diode, while focussing of intense lithium beams is under development. The beam parameters during this target experiment were not measured directly because the target geometry and diagnostic package were optimized for target response, rather than determining the focal quality of the beam. Nominal parameters on shots with similar diode voltage and current were determined with an extensive array of

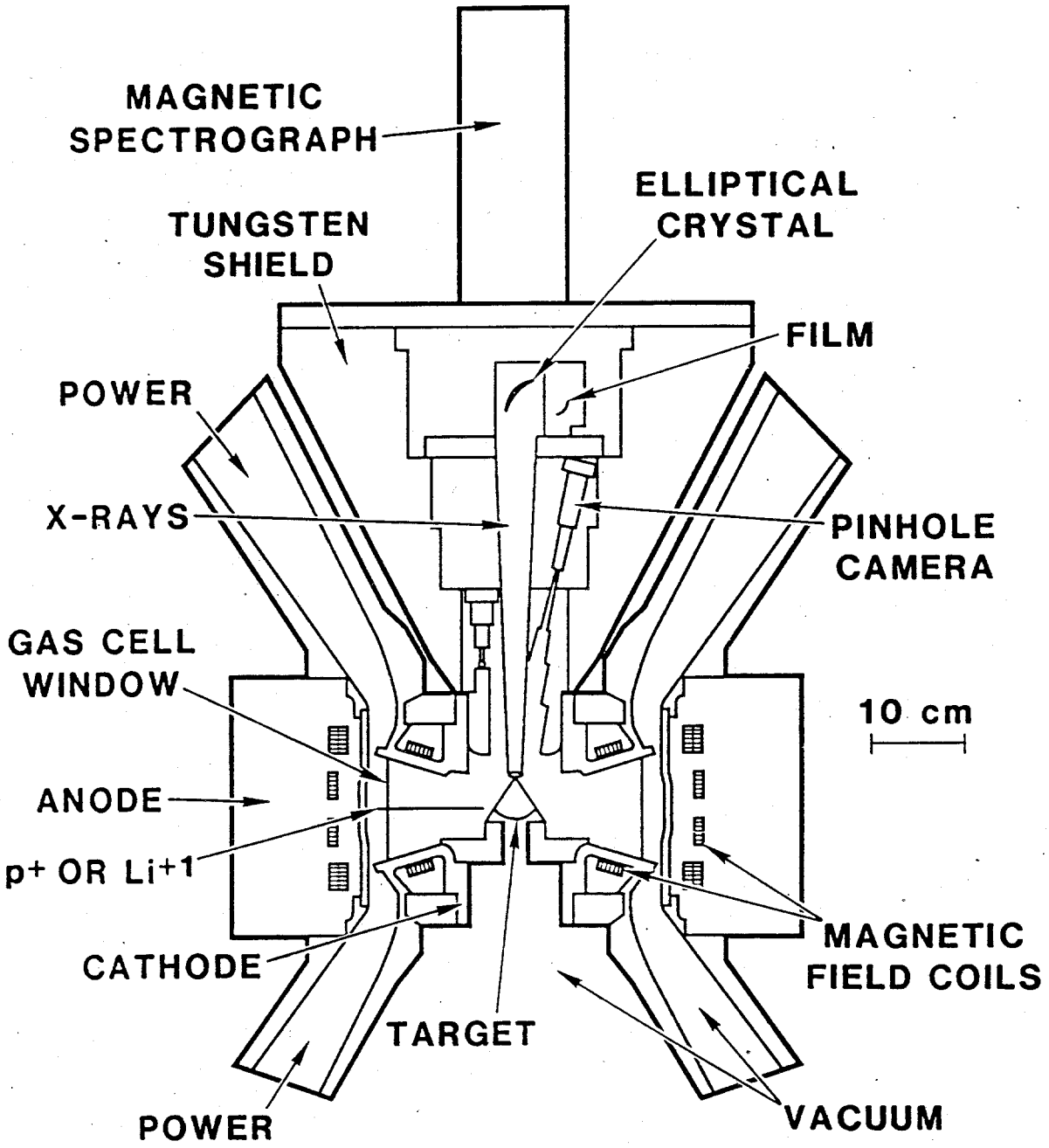

Figure 1. Schematic of the PBFA-II diode region. The diagnostics are packaged inside a tungsten shield to protect them from the hard x-ray background.

beam diagnostics [13]. These shots delivered 50-75 kJ of protons to a 1 cm diameter spot with a pulse width of 15-20 ns and a voltage at peak ion power of 4-6 MV. The specific power density incident on the target described in this paper was thus approximately 50-100 TW/g, providing a unique opportunity for exploring ion beam heated matter.

The x-ray spectrograph used for this experiment is designed to obtain high spectral resolution while coping with the severe experimental environment on PBFA-II. The rate of performing experiments on PBFA-II is presently limited to one per day. Another difficulty is the 5-10 MeV endpoint bremsstrahlung, generated by electron losses in the diode, that bathes instruments 1 m from the diode with a dose rate of $10^{12} - 10^{13}$ Rad(Si)/s. We overcome this problem by using a 1000 kg tungsten housing to provide about 10 cm of shielding around the spectrograph.

Time-integrated space-resolved x-ray spectra are acquired on PBFA-II using an elliptical crystal spectrograph [14] operated in the Johann focussing mode [14-16]. This essentially renders source broadening negligible, a crucial consideration since the scale size of the plasma heated by the ion beam is of order 1 cm, in contrast to laser-produced plasmas which are typically of order 100 μm. The elliptical geometry also has the advantage that the detector is isolated from the line of sight by the structure of the slit placed at the ellipse focus, reducing both the debris and the scattered x-rays incident on the detector. This is important because the debris created by the large energy delivered to the diode routinely destroys the x-ray crystal, but the elliptical geometry preserves the detector. A 0.5 mm space-resolving slit provides 1 mm space resolution at the target (magnification = 1), in addition to reducing the debris which enters the instrument itself. The PET crystal was curved [17] to an ellipse with eccentricity 0.9188 and height parameter 4.1656 cm. The range covered in first order was 6.4-8.66 Å. The experimentally-determined spectral resolution was $\lambda/\Delta\lambda > 1200$. The spectrum was recorded on Kodak DEF film, developed 5 min in Kodak Liquid X-Ray developer at

68°F. The data below is corrected for the film response [18,19], including the dependence on the angle of incidence in the Johann geometry.

A K_α spectrum from an aluminum target heated by the PBFA-II ion beam is shown in Fig. 2. The target was a 75 μm thick aluminum cone, with a half-angle of 15° and a midplane diameter of 14 mm. This thickness corresponds to one-half the range of 5 MeV protons in the cold material. The satellites corresponding to an increasing number of L-shell vacancies are clearly visible in Fig. 2. Analysis described in Ref. 8 ruled out the possibility that the satellites could have been produced via multiple ionization induced by carbon contamination in the beam. These satellites thus are due to vacancies produced by thermal ionization in the target, followed by proton-induced inner-shell ionization. The labeling of the satellite peaks corresponds to the ionization stage prior to the inner-shell ionization; the details of the line identifications are given below.

The wavelength scale in Fig. 2 is applied using the properties of the elliptical geometry, with the Al I K_α line (8.340 Å) serving as the standard. Imperfections in the Johann curve or the ellipse may cause deviations of the wavelength scale from the expected functional dependence. Calibration spectra obtained using a Manson source were used to evaluate the accuracy of the wavelength scale. We found that in the region 7.9-8.34 Å, the wavelengths were accurate to better than ±4 mÅ. In addition, there is a wavelength uncertainty due to the assignment of the peak intensity of the strongest line in the PBFA-II spectrum to be Al I. It is possible that the peak intensity actually corresponds to a higher ionization state (e.g., Al II or III), which would result in a systematic red shift of the entire spectrum by 2-3 mÅ [20]. The total experimental wavelength uncertainty is therefore comparable to the uncertainty in the theoretical wavelength predictions described below.

An estimate of the absolute measured photon flux emitted by the target was made in order to assist in interpreting the target opacity. We used the geometrical factors given

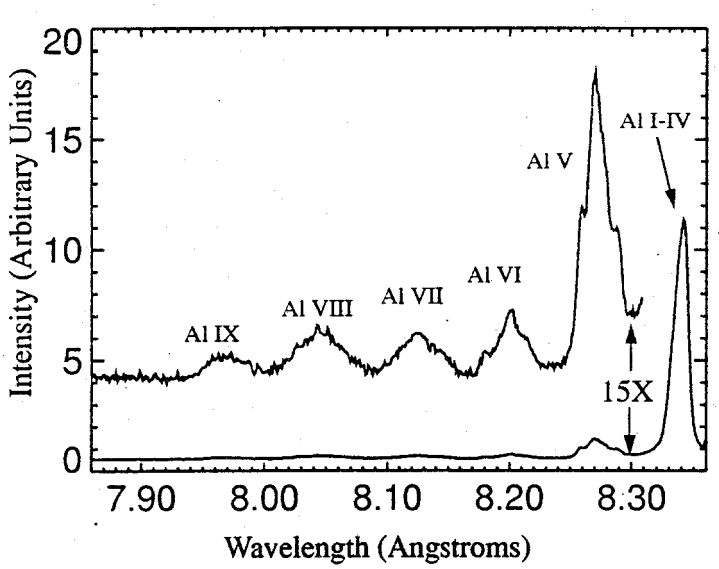

Figure 2. K_α spectrum from aluminum target irradiated by the PBFA-II ion beam. The top spectrum is the same as the bottom spectrum, but with the amplitude multiplied by a factor of 15. The labels refer to the ionization stages prior to beam-induced inner-shell ionization.

in Ref. 18 and a crystal reflectivity of 0.5 mR [21]. Assuming uniform emission into 4π, the energy emitted in the Al I–IV line was estimated to be 0.16 J. The faintest line emission observed was about 2 mJ (the peak labeled Al VIII in Fig. 2), close to the estimated threshold for detection with this instrument. In the absence of an absolute calibration, these estimates are probably reliable to a factor of three.

III. Theoretical Models

To study the physical processes affecting the K_α spectrum we have used a combination of atomic physics, collisional-radiative equilibrium, and hydrodynamics codes. We now briefly describe the major features of each model.

A. CRE Model

In our CRE model atomic level populations are determined by solving multilevel, steady-state atomic rate equations [22]. Transitions considered include collisional

excitation, deexcitation, ionization, and recombination; radiative and dielectronic recombination; and spontaneous decay. We also include the effects of the beam (proton beam impact ionization of inner-shell electrons and autoionization), and in some cases, the radiation field (photoexcitation and photoionization). In this detailed configuration accounting model each state of a given ion was coupled to all other states (ground and excited) of that ion, as well as all states of the next high ionization stage. Radiation is transported using either of 2 models: (1) an angle- and frequency-averaged escape probability model [22,23], or (2) a multiangle, multifrequency model [24] which solves a second order form of the transfer equation.

To compute spectral properties we consider emission and absorption from bound-bound, bound-free (including inner-shell attenuation), and free-free transitions. Voigt line profiles are used which include the effects of natural, Auger, Doppler, and Stark broadening. In the CRE calculation, Stark line broadening is modeled in the electron impact approximation. The semiclassical model of Griem [25] is used in conjunction with Hartree-Fock results for radial matrix elements and transition energies to the nearest dipole-allowed levels. More detailed Stark broadened line profiles were computed for some of the K_α lines; these results will be presented in Section IV.

The proton-impact ionization rate can be expressed as

$$R^P_{ii^*} = n_i \, J \, \sigma_K(E_B) \, , \tag{1}$$

where J is the current density, σ_K is the K-shell ionization cross section, E_B is the beam energy, n_i is the number density of particles in the initial state i, and i^* represents the index of the final (autoionizing) state. In the CRE calculations described below we have assumed the beam to be spatially uniform and monoenergetic. Autoionizing states are depopulated by two mechanisms: a resonance fluorescence in which a photon of energy ≈ 1.5 keV is emitted, or an autoionization in which a second electron is ejected. The two

rates are given by:

$$\begin{aligned} R_{i^*j} &= n_{i^*}\, A_{i^*j} && \text{(fluorescence)} \\ R_{i^*\kappa} &= n_i^* \left(\tfrac{1-Y_{i^*}}{Y_{i^*}}\right) \textstyle\sum_j A_{i^*j} && \text{(autoionization)} \end{aligned} \tag{2}$$

where A_{i^*j} is the Einstein coefficient for $i^* \rightarrow j$, and Y_{i^*} represents the fluorescence yield. For each ionization stage we have used the configuration-averaged fluorescence yields of McGuire, which are tabulated in Ref. 26. The final state of all autoionization transitions, κ, is assumed to be the ground state of the next higher ionization stage (for Al, multi-electron ejection via Coster-Kronig transitions is unimportant).

B. Atomic Physics Models

In our spectral calculations two different model atoms were used: one with fewer atomic levels and higher accuracy, the other with more levels but less accuracy. In the first case, our Al model atom consisted of 184 levels distributed over all 14 ionization stages. Of these 34 were autoionizing levels (Al I-XI ions with K-shell vacancies). Atomic structure calculations for levels involving K_α transitions were performed using a multiconfiguration Hartree-Fock (MCHF) code [27] with relativistic mass and Darwin corrections [28]. An L-S coupling scheme was used to define the angular momentum coupling of electrons. Details of these calculations are presented elsewhere [29]. The purpose of these calculations was to confidently determine the transitions most responsible for the observed peaks in the PBFA-II spectrum. Our second model atom consisted of a total of 750 energy levels distributed over all ionization stages. Roughly half of these were autoionizing levels. The additional levels primarily included excited state configurations with valence electrons in the $n = 3$ shell and their autoionizing counterparts. For this second data set, single configuration Hartree-Fock (SCHF) calculations were performed for all levels to determine transition energies and oscillator strengths. Reasonably accurate transition energies were obtained by including relativistic

corrections for levels in ground state configurations. For excited state configurations no corrections were made as it was assumed that blue-shifting relativistic corrections are essentially cancelled by red-shifting electron correlation interactions [29]. Using this model we find good agreement with other published experimental results [7], indicating these approximations are quite reasonable.

Rate coefficients for collisional and radiative transitions were calculated as follows. Collisional excitation and ionization rates were computed using a combination of semiclassical impact parameter, Born-Oppenheimer, and distorted wave models [30-32]. The corresponding inverse processes were specified from detailed balance arguments. Rate coefficients for dielectronic recombination were computed using a Burgess-Mertz model [33] in conjunction with Hartree-Fock energies and oscillator strengths. Photoionization cross sections and radiative recombination rates were obtained from Hartree-Fock calculations.

Proton impact ionization of K-shell electrons were calculated for each ionization stage of Al using a plane wave Born approximation (PWBA) model [34]. Computed cross sections for Al I, Al V, and Al X are shown in Fig. 3 as a function of proton energy. Also shown are experimental data for Al I [35,36]. The differences between the calculated and experimental data for Al I are seen to be comparable to the differences between the two sets of experimental data ($\sim$ a few tens of percent) at proton energies relevant to the PBFA-II experiment (> 1 MeV). Our calculations indicate that the cross section decreases with increasing ionization stage in a roughly linear fashion. A linear approximation was used in our CRE calculations.

C. Hydrodynamic and Beam Energy Deposition Models

Input required for performing the hydrodynamic simulations is an energy source term which describes the ion beam heating of the target. This was obtained by performing transport simulations for the experimental diode voltage and currents using the PICDIAG

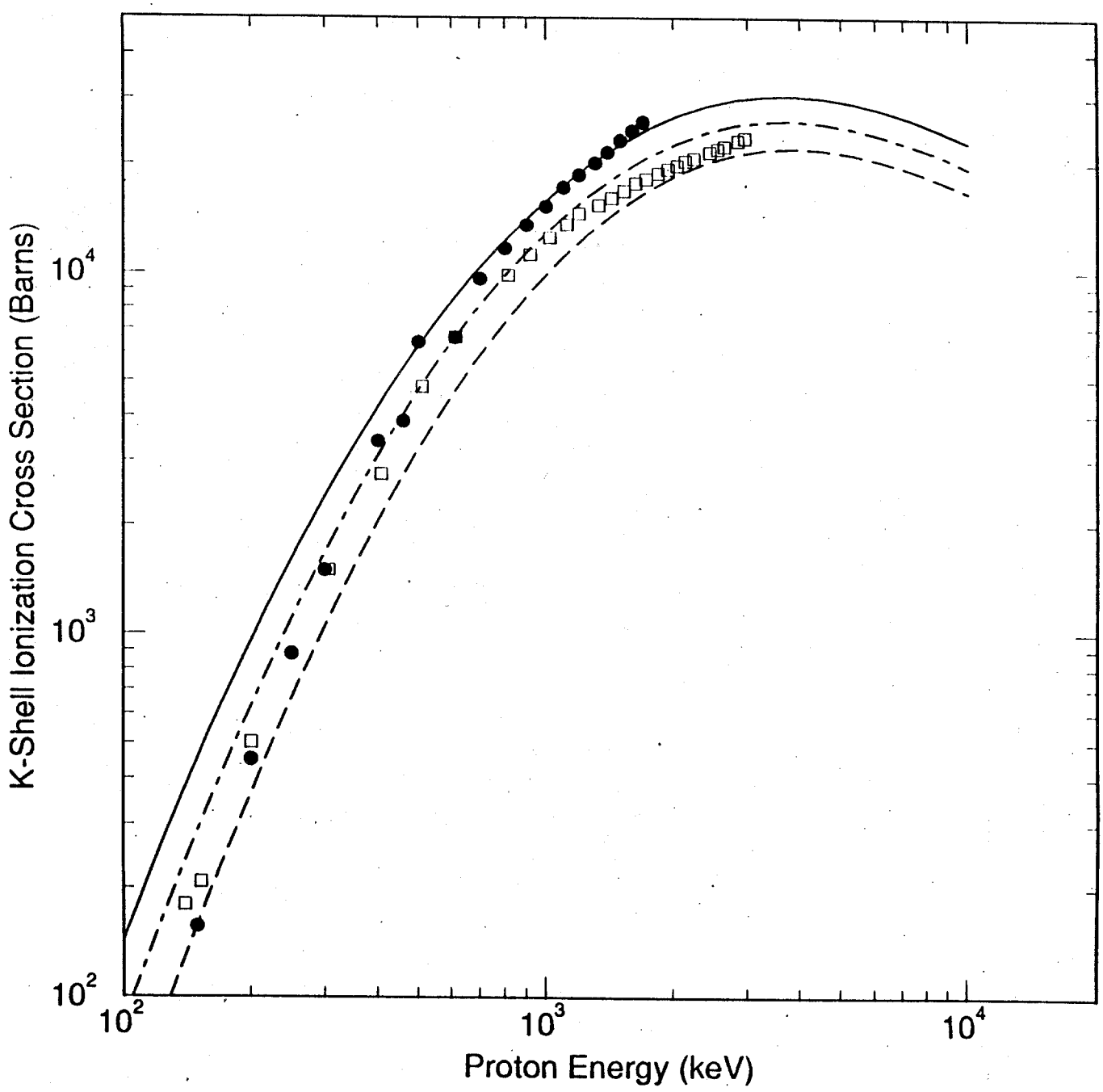

Figure 3. K-shell proton impact ionization cross sections calculated for Al I (solid curve), Al VI (dash-dotted curve), and Al IX (dashed curve). Also shown are experimental data for Al I from Ref. 35 (□) and Ref. 36 (●).

code [37] to determine the ion energy and intensity time histories of the beam striking the Al cone. Input to these simulations included the experimental geometry, such as the anode shape and gas cell configuration, as well as the diode voltage and currents for the specific shot. Beam divergence, current neutralization fractions, and ion species information from related setup shots were used. The effects of applied- and self-field bending of the multispecies ion beam were included in the simulations, as were the effects of finite source divergence, multiple scattering during transport, and time-of-flight dispersion.

The target was modeled as a cylinder with a diameter equal to that of the cone midplane. Time- and space-dependent ion energies and beam intensities were tallied at the target location for each ion species. This information was then used as input to the hydrodynamic simulations.

A 1-D radiation-hydrodynamics code was used to calculate the time history of the temperature and density distributions in the target plasma. An analytic equation of state was used for the Al plasma. The spatial dependence of the ion energy deposition was calculated for each species of the ion beam using a ion stopping model [38] which includes the effects of collisions between ions and free electrons in a hot plasma (range shortening effect).

IV. Physical Processes Affecting K_α Spectral Emission

A. Role of Excited State Transitions

K_α line radiation in light ion beam experiments is emitted as a result of two processes: ion-impact ionization of a $1s$ electron followed by a spontaneous fluorescence transition. We now examine the production of K_α line emission from ions of excited state configurations. (The role of such configurations in absorption experiments was recently

reported in Ref. 6.) Consider the transition:

$$1s^2\,2s^2\,2p^3\,3\ell \underset{p-impact}{\rightarrow} 1s^1\,2s^2\,2p^3\,3\ell \underset{K_\alpha}{\rightarrow} 1s^2\,2s^2\,2p^2\,3\ell$$

where ℓ represents an s, p, or d subshell. K_α lines of this type differ in 2 important respects from those produced by ions originally in ground state configurations. First, the wavelength of a transition involving excited states is similar to that for a low-lying level of the next higher ionization stage. This occurs because the valence electron in the outer shell has little effect on the electronic wavefunctions in the inner regions of the ion (an effect analogous to the Li-like dielectronic satellites which commonly appear in laser-produced plasma spectral lines on the long-wavelength side of the He-like resonance lines). This is illustrated in Fig. 4, where stick spectra (oscillator strength vs. wavelength) of the K_α lines for Al I-IX are shown. The ions are referred to by their stage prior to ion-impact ionization. The wavelengths were obtained from the SCHF calculations described above. The wavelength regions dominated by excited state configurations are bracketed by arrows while the remaining lines generally involve ground state and low-lying excitation state configurations. Looking at the region near 8.2 Å it is clear that many excited state lines from Al V reside in the same wavelength region as those from low-lying states of Al VI.

The second important difference between these two types of lines is that the plasma broadening effect on the lines involving excited states can be considerably larger. To study this effect in detail we have performed Stark broadened line profile calculations using a recently developed multielectron line shape formalism and code [39,40]. Broadening effects due to both electrons and ions were considered. The electron broadening effect was computed using a second order quantum relaxation theory while ion broadening was calculated using a microfield distribution function and the static ion approximation. In these calculations atomic physics data was computed using the atomic structure codes of Cowan and included multiconfiguration effects [41].

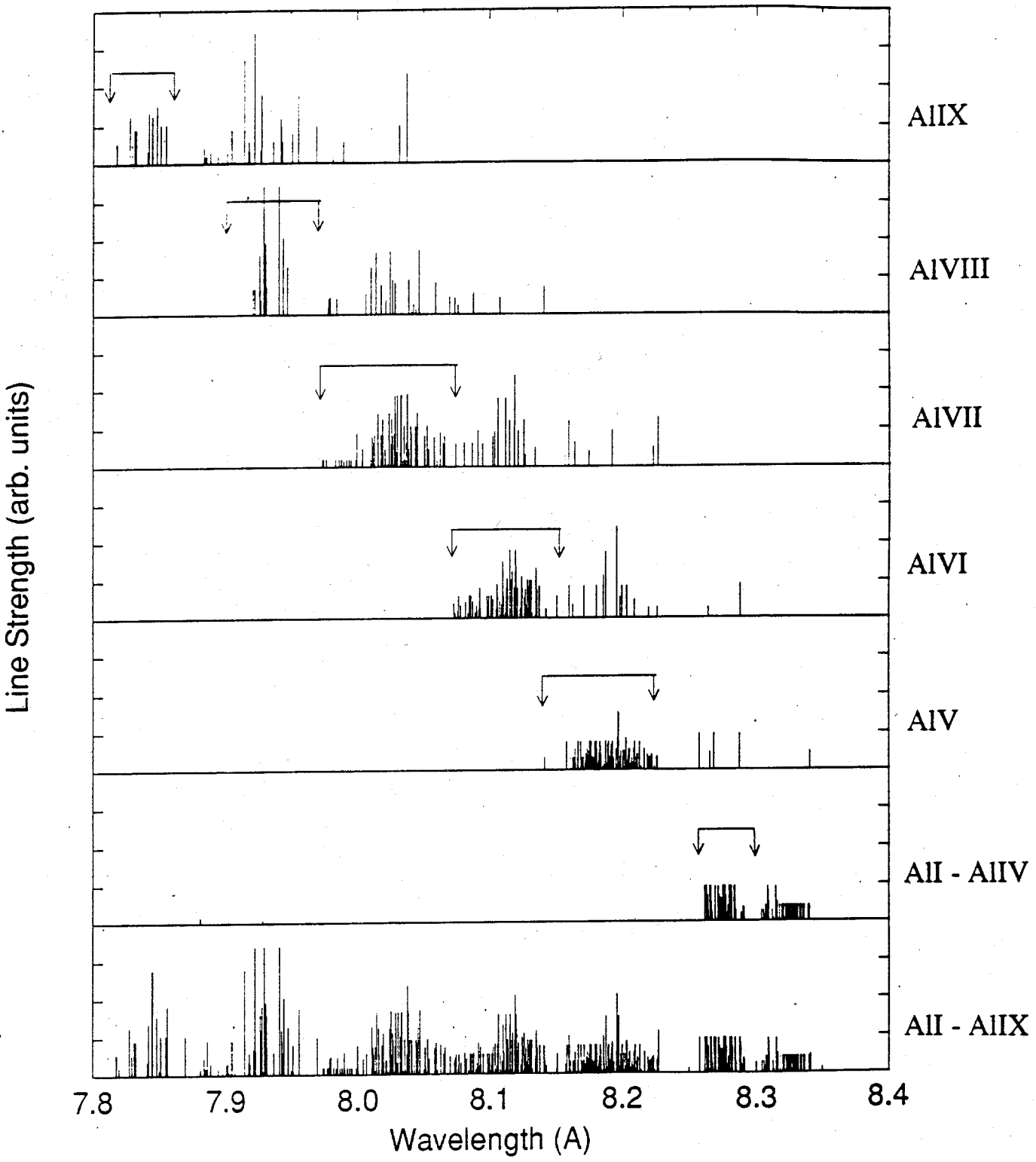

Figure 4. Stick spectrum showing K_α line wavelengths for Al I–IX. The regions bracketted by arrows represent wavelength regions dominated by excited state configurations (with $n = 3$ valence electrons).

Figure 5 shows results from several sets of line profile calculations for low-lying states of O-like and F-like Al (Al V and IV prior to ion-impact ionization, respectively; in this paper we shall refer to the ionization stage after inner-shell ionization as O-like, F-like, etc., and the stages prior to inner-shell ionization as Al V, Al VI, etc.). The line shapes are area normalized; opacity effects are not included. Figure 5(a) shows the contribution from several broadening mechanisms for the K_α lines of O-like Al at $T = 20$ V and $n_e = 10^{23}$ cm^{-3}. For these calculations, 6 upper energy levels (corresponding to configurations $1s^1\,2s^2\,2p^5$ and $1s^1\,2s^1\,2p^6$) and 10 lower energy levels (corresponding to configurations $1s^2\,2s^2\,2p^4$, $1s^2\,2s^1\,2p^5$, and $1s^2\,2p^6$) were considered. The relative transition strengths were calculated assuming LTE. The 3 prominent features are dominated by transitions from upper energy levels in the configuration $1s^1\,2s^2\,2p^5$. The solid curve includes the effects of Stark and Doppler broadening. The long-dashed curve includes the additional effects due to the widths associated with radiative and Auger decay using the model described in Ref. 42. The widths associated with Doppler broadening and radiative decay are relatively small (0.6 mÅ and 0.06 – 0.16 mÅ, respectively). However, the Auger decay effects are much larger (widths ∼1.6 – 2.2 mÅ) and have a significant impact on the line shape. The short-dashed line represents the profile convolved with a Gaussian of 5.3 mÅ FWHM to approximate instrumental broadening effects in the PBFA-II experiment. Figure 5(b) shows a series of calculations at different densities for O-like Al with all broadening effects described above included. It is clear from these results that Stark broadening is not important for these lines at electron densities below about 2×10^{23} cm^{-3}. At the lower densities the Auger and eventually, instrumental widths dominate.

Figure 5(c) shows the density sensitivity of line profiles for transitions arising in excited state configurations of F-like Al; that is, with one spectator electron in the $n = 3$ shell. Upper energy levels of these transitions have configurations of the type

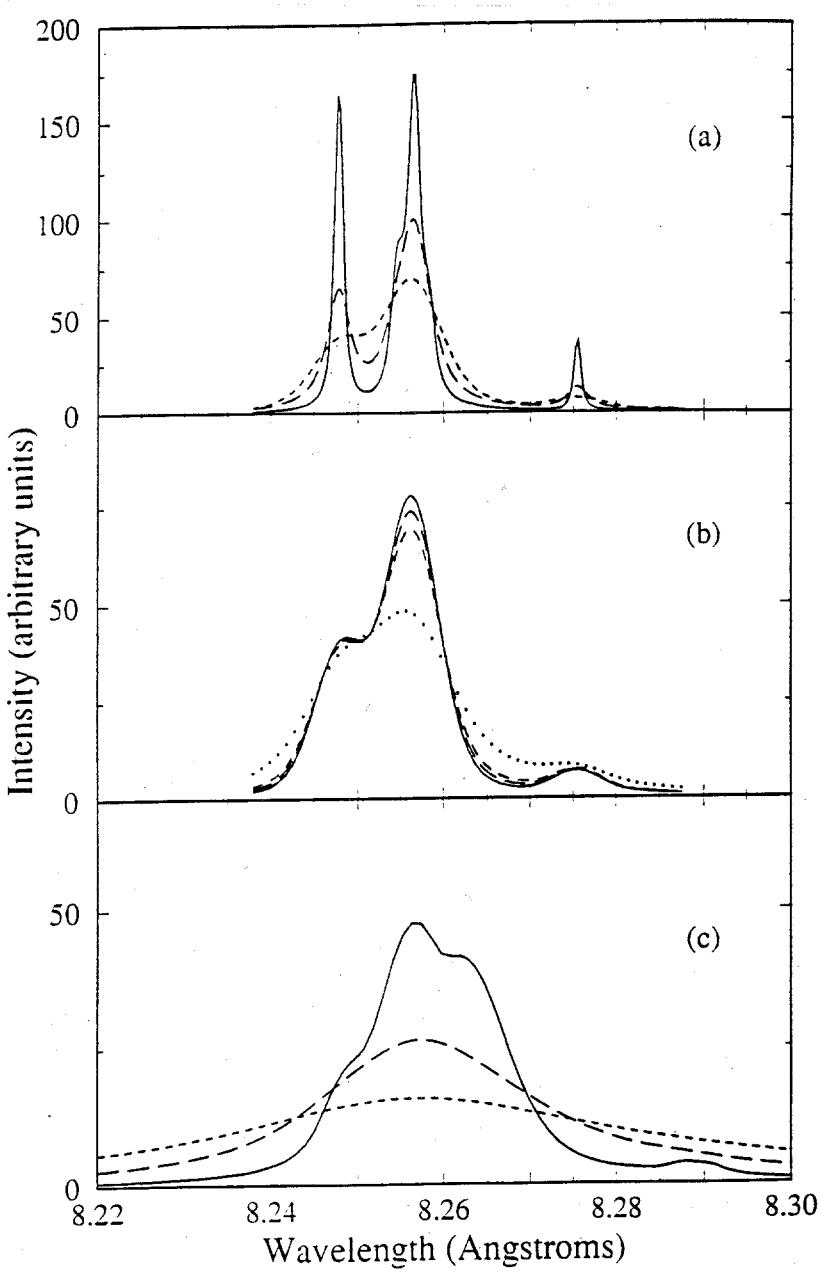

Figure 5. (a) Line profiles for K_α transitions in O-like Al at $T = 20$ eV and $n_e = 10^{23}$ cm^{-3}: (solid) Stark plus Doppler broadening; (long-dashed) same as solid but also includes Auger and radiative decay widths; (short-dashed) same as long-dashed but with instrumental broadening. (b) Stark broadened line profiles at $T = 20$ eV including Auger and radiative decay widths, and instrumental broadening for $n_e = 1\times10^{22}$ cm^{-3} (solid), 5×10^{22} cm^{-3} (long-dashed), 1×10^{23} cm^{-3} (short-dashed), and 5×10^{23} cm^{-3} (dotted). (c) Stark broadened profiles in F-like Al with one spectator electron in $n = 3$ shell at $T = 20$ eV and $n_e = 5\times10^{21}$ cm^{-3} (solid), 2×10^{22} cm^{-3} (long-dashed), and 5×10^{22} cm^{-3} (short-dashed).

$1s^1\,2s^2\,2p^5\,3\ell$ and $1s^1\,2s^1\,2p^6\,3\ell\,(\ell = s, p, d)$. The spectrum is dominated by transitions coming from the $1s^1\,2s^2\,2p^5\,3\ell$ configuration. For the results displayed in Fig. 5(c) we considered 48 upper energy levels of the type $1s^1\,2s^2\,2p^5\,3\ell$ and 57 lower energy levels of the type $1s^2\,2s^2\,2p^4\,3\ell$. These lines show a much more pronounced dependence on electron density than those for the O-like case at these densities. The presence of the $n = 3$ electron makes these states easier to perturb by the plasma microfields. Thus, the K_α lines resulting from excited state configurations offer better opportunities for diagnosing plasma densities in the range of densities relevant to the PBFA-II experiment.

To determine whether lines from excited state configurations should make a significant (observable) contribution to K_α emission spectra obtained in light ion beam experiments, we performed two CRE calculations which were identical except for the number of autoionizing states in our atomic model. In the first calculation only autoionizing states which originated as ground state configurations were considered, while in the second calculation we included autoionizing states of the type $1s^1\,2s^1\,2p^{w-1}$ and $1s^1\,(2s\,2p)^{w-1}3\ell$. In the latter case a total of 624 energy levels were considered in the atomic model. In each calculation the plasma was assumed to be a planar slab of width $L = 0.1$ μm, $T = 30$ eV, and $n = 10^{-1}\,n_0$ ($n_0 \equiv$ solid density).

The resulting spectra are shown in Fig. 6. Comparison of the spectra calculated with (solid curve) and without (dotted curve) excited state configurations included shows that excited states are clearly important contributors. In addition to more relatively narrow features appearing in the spectrum from $1s^1\,2s^1\;2p^{w-1}$ configurations, broader features from the $1s^1\,(2s\,2p)^{w-1}3\ell$ configurations are very apparent.

As a direct comparison with the time-integrated PBFA-II spectrum a similar set of calculations was performed for the following conditions: $T = 20$ eV, $n = 10^{-1}\,n_0$, and $L = 100$ μm. (These conditions are consistent with those predicted from hydrodynamic simulations of the PBFA-II experiment.) In the first calculation we used the MCHF

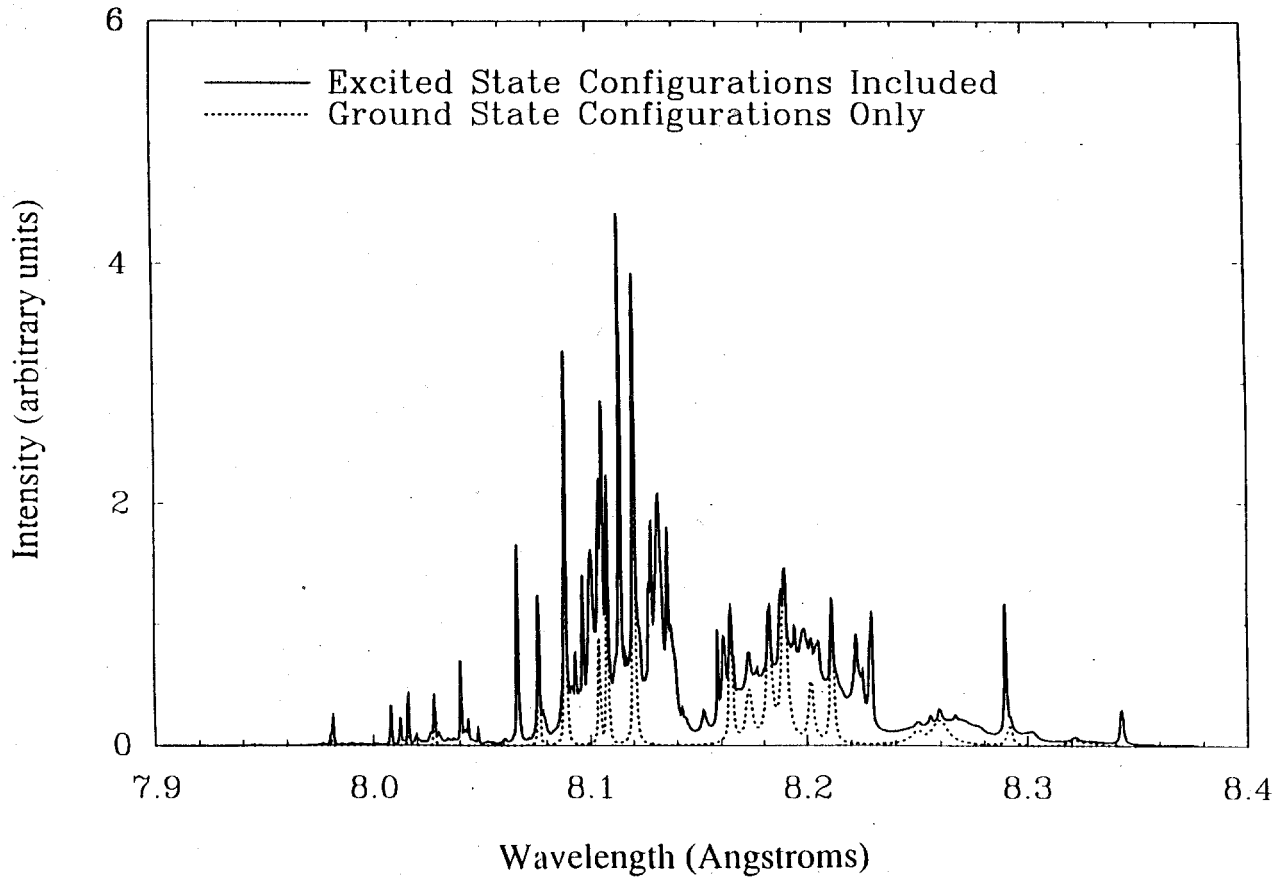

Figure 6. Calculated K_α emission spectrum for an Al plasma at $T = 30$ eV, $n = 10^{-1}\, n_0$, and $L = 0.1\,\mu$m; (dotted) includes ground state configurations only; (solid) also includes excited state configurations up to $n = 3$.

atomic data set which included only low-lying and ground state configurations. Figure 7 shows the calculated (short-dashed curve) and experimental (solid curve) spectra in the narrow wavelength range which corresponds to emission from the ground state configuration of Al V. Note that the calculated spectrum exhibits much more narrow and pronounced peaks than the observed spectrum. The peak resulting from the $^1P \rightarrow\ ^1S$ transition is slightly higher than that of the $^1P \rightarrow\ ^1D$ transition — just the opposite of what is observed in the experiment. It is also clear that in this calculation the intensity between the peaks is much lower than observed.

In the second calculation we used the SCHF data set, which is slightly less accurate but included many more excitation levels. The calculated spectrum for this case is given by the dashed line in Fig. 7. The most noticeable feature from this calculation is that the intensity between the peaks is filled in by K_α transitions involving excited states. This radiation is due to the superposition of many broad lines produced by transitions of the type $1s^1\,2s^2\,2p^5\,3\ell \rightarrow 1s^2\,2s^2\,2p^4\,3\ell$ and $1s^1\,2s^1\,2p^6\,3\ell \rightarrow 1s^2\,2s^1\,2p^5\,3\ell$. It is also seen that the peak of the $^1P \rightarrow\ ^1S$ line is lower than that of the $^1P \rightarrow\ ^1D$ line, which is in qualitative agreement with the experimental spectrum. This is caused by greater opacity for the $^1P \rightarrow\ ^1S$ line arising from the other relatively broad lines. The calculated spectrum in this case shows the $^3P \rightarrow\ ^3P$ and $^1P \rightarrow\ ^1D$ lines to be somewhat narrow compared to experiment. This, at least in part, is due to instrumental broadening, which is not included in these calculations. Note, however, that instrumental broadening is not sufficient to fill the gaps between the peaks (see Fig. 5(a)) when excited states are not included.

B. Opacity Effects

In the PBFA-II experiment the thickness of the conical Al target was 75 μm, which is approximately equal to the half-range of 5 MeV protons in cold Al. This leads to two significant sources of opacity. First, the continuum optical depth due to L-shell

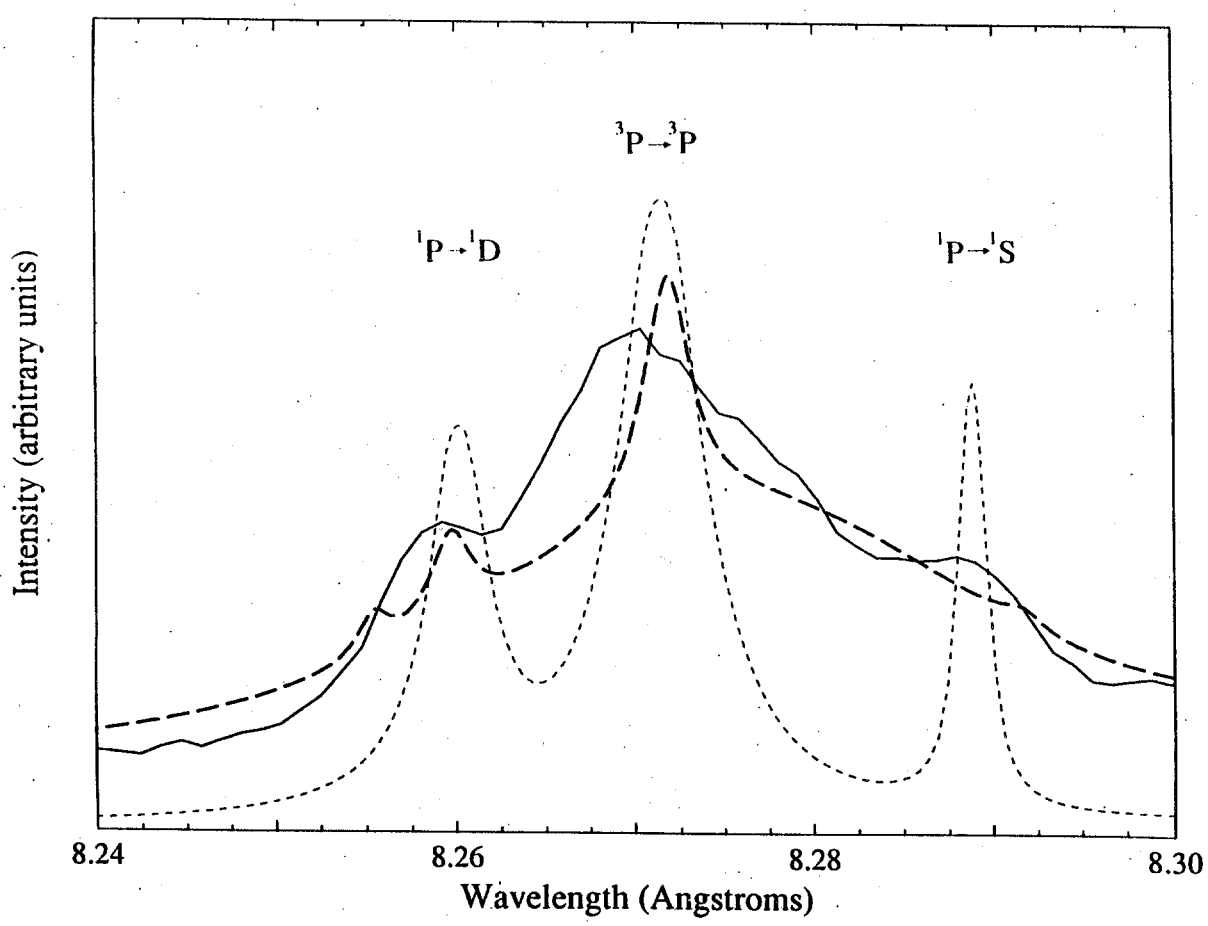

Figure 7. Comparison of calculated and experimental K_α spectra in region dominated by ground state configurations of O-like Al (prominent features are labelled) and excited states of F-like Al: (solid) experimental spectrum; (long-dashed) calculation including $n = 3$ excited state configurations; (short-dashed) calculation with ground state configurations only.

photoabsorption for this thickness is about $7-8$ over the frequency range of K_α emission. Because of this the spectrometer, which was located above the top of the cone, could see only those photons emitted from the outer "skin" of the plasma. Second, we find that optical depths for the K_α lines range up to $10^3 - 10^4$. This indicates that resonant self-absorption had a very significant impact on the observed spectrum.

One of the effects line opacity has is to skew the observed spectrum toward higher ionization stages [9]. That is, ions with ionization stage higher than the most abundant stage can emit the greatest flux. This is shown in Fig. 8, where the calculated spectral intensity is plotted for planar Al plasmas of varying thickness. In each case the temperature was 35 eV and the density was $10^{-2}\, n_0$. The plasma thickness ranged from 10^{-4} cm to 1 cm, which corresponds to a solid density thickness of 100 Å to 100 μm. For the $L = 10^{-4}$ cm case, the optical depth at all frequencies was less than unity, and was greater than 10^{-1} for only the strongest lines. Therefore opacity has a relatively minor effect on its spectrum. In this case, the peak intensities come from N-like and C-like Al, which originate from the most abundant ionization stages. As the plasma thickness increases, the intensities of the B-like and Be-like Al lines increase, while those of the N-like and C-like Al lines do not because their optical depths exceed unity at $L \gtrsim 10^{-3}$ cm. (Note that the $L = 10^{-4}$ and $L = 10^{-2}$ intensities have been multiplied by 30 and 1.5, respectively.) For the $L = 1$ cm case B- and Be-like lines exhibit the greatest intensities even though they originate from ions whose fractions are calculated to be 0.10 and 0.007, respectively.

The optical depth for the $L = 1$ cm case is plotted in Fig. 9 as a function of wavelength. Optical depths are measured along a line of sight normal to the plane of the plasma. The optical depths are greatest for O-like and N-like lines. Even the strongest B-like lines — which involve $1s^1\, 2s^1\, 2p^2 \rightarrow 1s^2\, 2s^1\, 2p^1$ transitions — have optical depths ranging to $\sim 10^2$. The continuum optical depth from L-shell photoabsorption is

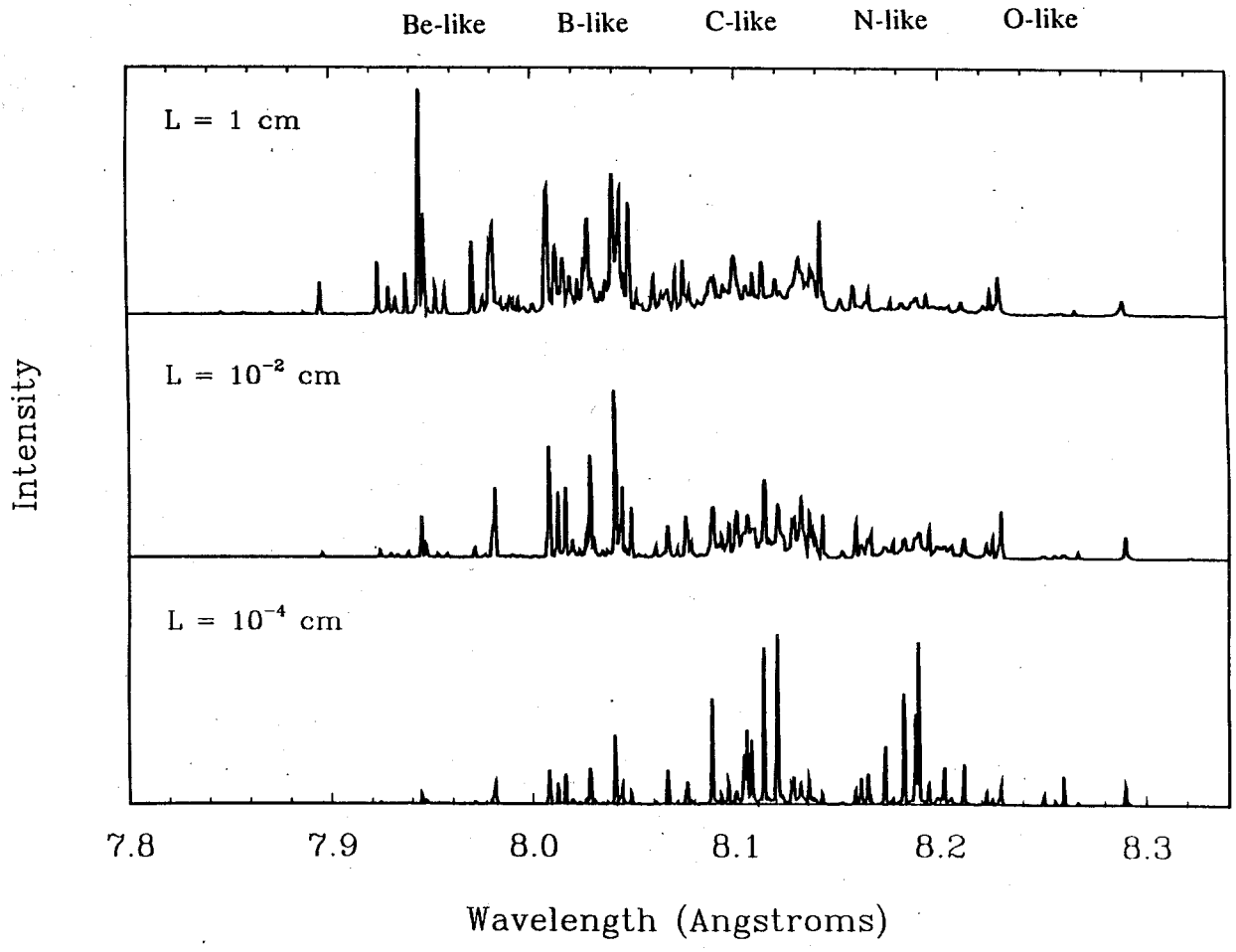

Figure 8. Calculated K_α spectra for Al plasmas at $T = 35$ eV and $n = 10^{-2}\, n_0$. Widths of the plane-parallel plasmas range from $L = 1\,\mu$m (bottom) to 1 cm (top). Opacity effects tend to skew the spectrum toward higher ionization stages. $L = 10^{-2}$ cm and $L = 10^{-4}$ cm intensities are multiplied by 1.5 and 30, respectively. The labels refer to the ionization stage after beam-induced inner-shell ionization.

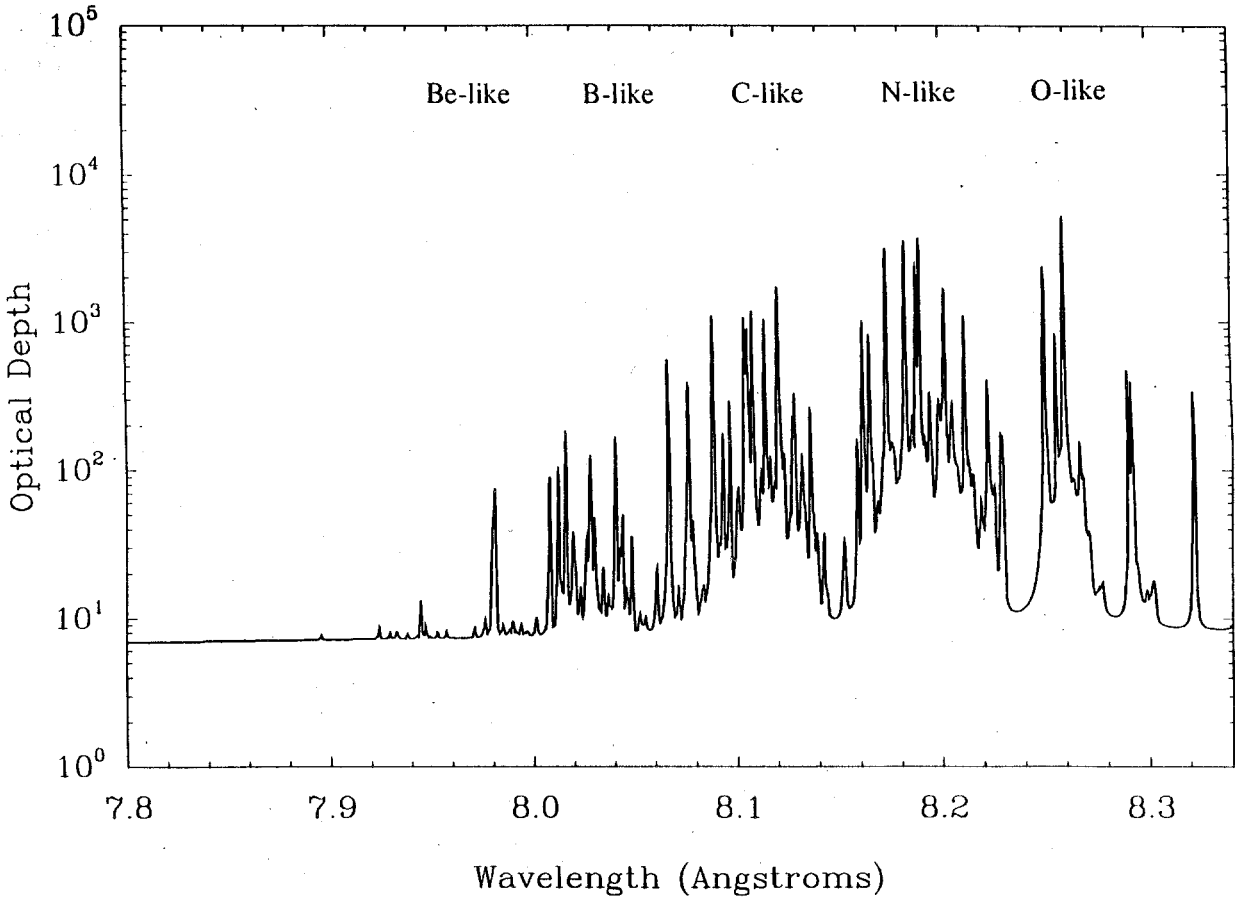

Figure 9. Wavelength dependent optical depth for the $L = 1$ cm case in Figure 8.

about 7 – 8. The L-shell photoabsorption cross section is not extremely sensitive to ionization stage for Al I - Al X, and therefore the continuum opacity is only a weak function of the temperature. It is also important to note that for targets $\gtrsim 10^2\,\mu$m thick the continuum opacity can significantly affect the observed line profiles. This causes additional complications when trying to deduce plasma conditions from individual line profiles.

V. Numerical Simulations of PBFA-II Experiment

In the radiation-hydrodynamic simulations the Al cone was modeled in 1-D as a 75-μm thick, 14-mm diameter cylinder with a central void. The target thickness corresponded to approximately one-half the range for protons at 5 MeV. Therefore, the protons initially deposit energy while travelling through one side of the cone and stopping in the other side. As the target is heated, the ion range decreases and the primary energy deposition then occurs only in the near side of the cone.

The current and particle flux of the carbon contaminant beam were $\lesssim 15\%$ and 5% of the total beam, respectively. Because of these seemingly low values only heating from protons was considered in our first series of calculations. These simulations, however, were not able to produce an electron temperature in the target plasma high enough to be consistent with the Al K_α satellite lines observed by the x-ray spectrometer. When heating by C^{+3} was added to the simulations the outer surface of the target plasma was heated to significantly higher temperatures. This occurs because C^{+3} ions have a significantly shorter stopping range than protons. Thus, the interior regions of the conical target were heated primarily by protons in these simulations while the outer skin was heated by carbon ions.

For our hydrodynamic simulations a peak proton intensity of 2.4 TW/cm^2 and a peak C^{+3} intensity of 0.7 TW/cm^2 were used. The time history for the C^{+3} ions was predicted from PICDIAG simulations. About two-thirds of the energy deposited in the

target was carried by the proton beam. However, since the carbon ions deposit their energy near the outer surface, they can have a strong effect on the temperature of that region. Because of the significant effect of opacity on the measured K_α spectrum, it is expected that the spectrometers observed emission only from the outermost skin of the target plasma.

Results from the radiation-hydrodynamic simulations which included effects of carbon heating are shown in Fig. 10. Shown are the temperature and density distributions as a function of radius at simulation times from 40 to 80 ns ($t = 0$ in the simulations corresponds to the time at which the machine is triggered.). The hollow cylindrical target starts at $r = 0.76$ cm and expands as it is heated. The peak temperatures in the interior regions of the target — i.e., the region heated by protons — are about 20 eV. The temperatures in the outermost regions reach a peak of about 55 eV at 90 ns. The maximum temperature in this region is attained at relatively late times because the peak current for the C ions lags that of the protons by about 25 to 30 ns. The target expands by a factor of roughly $10^2 - 10^3$ while the beam irradiates the target.

Using the results from the hydrodynamic simulations as a guide we performed a series of CRE calculations using characteristic plasma conditions at several stages of the target plasma evolution. The goal was to examine whether calculated spectra are consistent with the time-integrated experimental spectrum. In each case calculations were performed for isothermal slabs of width $L = 100\,\mu$m. (The results are insensitive to L if $L \gtrsim 30\,\mu$m because the plasma is optically thick at all wavelengths in the K_α spectral region.) For the purpose of calculating beam impact ionization, the beam was assumed to be a spatially uniform, monoenergetic beam of 5 MeV protons. The following parameters were chosen to represent early, middle, and late stages of the plasma evolution:

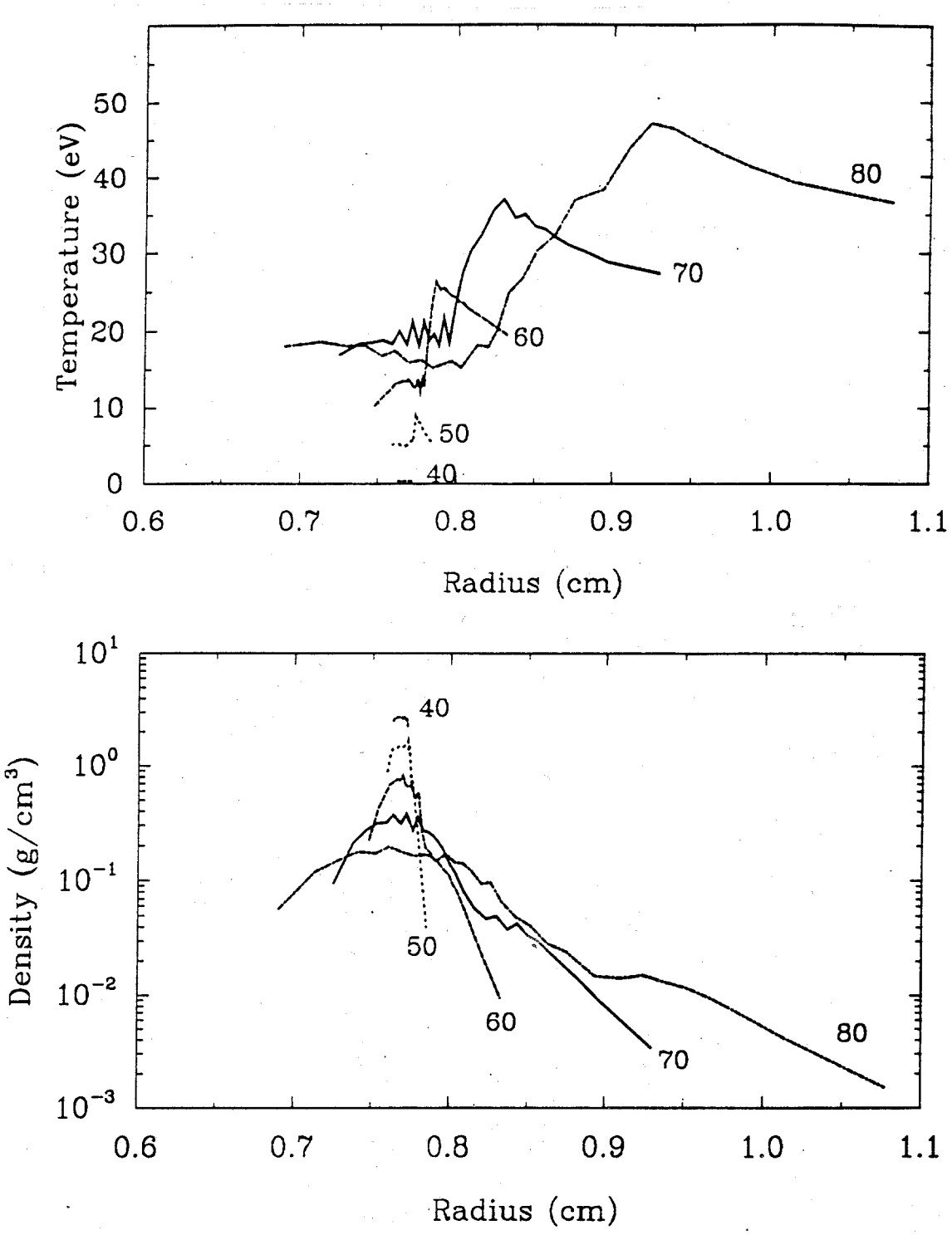

Figure 10. Time evolution of temperature (top) and density (bottom) distributions predicted from radiation-hydrodynamic simulations. The ion beam irradiates the target from the right in this figure. The curves are labelled by the simulation time in ns.

T (eV)	n/n_0	$J_{protons}$ (MA/cm^2)
2.5	0.20	0.15
25	0.05	0.30
35	0.01	0.30

These conditions correspond roughly to the C-heated region of the plasma at simulation times of 45, 60, and 70 ns. Plasma conditions corresponding to later times (higher temperatures) are not included here because: (1) the proton current — i.e., the particles most responsible for producing the K_α emission — drops significantly at the later times; and (2) higher temperatures produce K_α satellites at shorter wavelengths than those observed by the x-ray spectrometer. While the C ions may play a significant role in heating the outer skin of the plasma — which, due to opacity effects, is likely the source of K_α photons seen by the detector — proton-impact ionization is primarily responsible for the observed spectrum [8].

Figure 11 shows the emission spectra computed for the $T = 2.5$ eV (top), 25 eV (middle), and 35 eV (bottom) cases. Note that the scale for the $T = 2.5$ eV case is reduced by a factor of 10. At 2.5 eV, the dominant ionization stages are Al I and II. The K_α lines for these ions lie very close together and appear as a single feature. The radiation from these lines is not inhibited by opacity effects because there are very few ions with $2p$ vacancies at this temperature. Because of this, the intensities from K_α lines from the lowest ionization stages are about an order of magnitude higher than the satellites from higher ionization stages. This indicates that the large flux coming from the Al I–IV peak in the experimental spectrum (see Fig. 2) very likely occurred during the early phases of the plasma evolution when temperatures were $\lesssim 5$ eV.

For the $T = 25$ eV case the dominant ionization stage is Al IV. Despite this the highest intensity comes from K_α transitions in N-like Al which originates as Al VI. This effect is caused by resonant self-absorption. The line intensities in this case are ~ 10

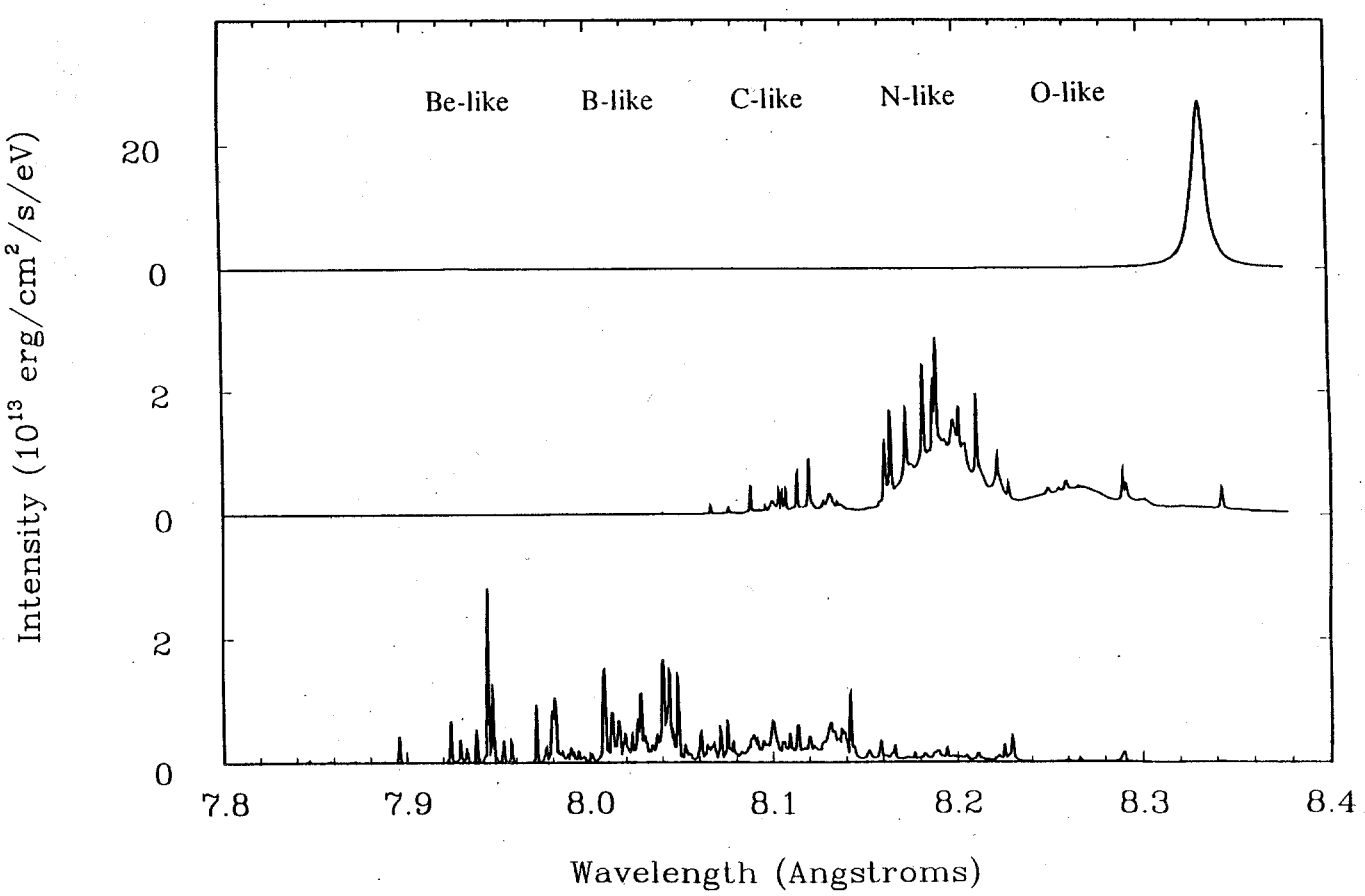

Figure 11. Calculated K_α spectra for Al plasmas with the following conditions: (top) $T = 2.5$ eV, $n = 0.2\,n_0$, $J = 0.15$ MA/cm^2; (middle) $T = 25$ eV, $n = 0.05\,n_0$, $J = 0.3$ MA/cm^2; (bottom) $T = 35$ eV, $n = 0.01\,n_0$, $J = 0.3$ MA/cm^2. Note the $T = 2.5$ eV intensities have been reduced by a factor of 10.

times lower than in the $T = 2.5$ eV case due to line opacity effects. The peak flux from the $T = 35$ eV case is from Be-like and B-like Al. This wavelength region — which may also contain contributions from lines originating from excited states of Al VIII — corresponds to the shortest wavelength peak observed in the PBFA-II spectrum. Similar calculations were run at several other densities ($n = 2 \times 10^{-3}\, n_0$ to $5 \times 10^{-2}\, n_0$) to find the range of temperatures at which an appreciable K_α flux appeared at $\lambda = 7.9$-8.0 Å, but not at shorter wavelengths. This temperature range was found to be 30 eV to 45 eV.

Because the continuum is optically thick the radiation measured by the spectrometer originated in the outermost regions of the expanding target plasma. We therefore expect that both the protons and carbon ions contributed to the *heating* of the target plasma regions observed by the spectrometer. Earlier analysis [8], however, suggests that the satellite line *emission* is primarily a product of proton-impact ionizations, as opposed to multiple ionization events produced by carbon ions. In addition, the carbon particle flux was believed to be only $\lesssim$ 5% of the proton flux in the experiment. This suggests that the plasma emitted K_α lines at a detectable level only while the proton current density was sufficiently high. Our calculations therefore suggest that temperatures of 30-45 eV were attained in the outer regions of the plasma while the proton current was relatively high. It remains possible that somewhat higher temperatures were reached either deeper inside the target plasma or at later times after the proton current dropped.

Because of the experimental complexities (e.g., geometry, opacity effects, time-integrated spectral measurements), a more detailed comparison of synthetic spectra with experiment has little added value at this time. We have demonstrated that computed K_α spectra, based on temperatures predicted from hydrodynamic simulations, are consistent with experimental measurements. In future experiments it is expected that time-resolved x-ray spectra will be obtained. Also, targets with thin tracer (diagnostic) layers or

dopants can be implanted in targets to provide additional spatial resolution and mitigate opacity effects. These features will make it possible to more precisely determine the evolution of target plasma conditions from x-ray spectra.

VI. Summary

We have reported on our analysis of the first spectroscopic observations of K_α x-ray satellites from a moderately ionized target heated by an intense ion beam. A combination of atomic physics, CRE, line broadening, and hydrodynamic calculations were performed to investigate the physical processes that affect K_α emission spectra, and to deduce the plasma conditions attained in the PBFA-II experiment. A primary goal of this investigation is to lay the groundwork for diagnosing plasma conditions from inner-shell line radiation in future light ion beam experiments.

We have studied the relative contributions of ground state and excited state configurations to K_α emission spectra. Lines originating from excited state configurations were shown to make a very significant contribution. Calculations performed with these configurations included produced much better agreement with the PBFA-II spectrum. Transitions originating in excited states with $n \geq 3$ electrons result in relatively broad K_α lines which are blue-shifted relative to those of ground state configurations. In addition, excited state lines tend to be primarily Stark broadened and are sensitive to the electron density. The line widths of K_α transitions involving ground and low-lying excited states are dominated primarily by Auger rates below densities of $n_e \approx 2 \times 10^{23}$ cm^{-3}.

Opacity was found to have a significant effect on the K_α emission spectrum. For Al targets with thicknesses $\sim 10^2\,\mu$m line optical depths were found to range as high as 10^4, while the continuum optical depth from L-shell photoabsorption was ~ 5 –10. This indicates that the photons observed by the spectrometer were emitted from the outer "skin" of the Al plasma. It was also shown that resonant self-absorption can lead to a

skewing of the K_α spectrum so that the intensities from lines of the dominant ionization stages are lower than those of less abundant higher ionization stages.

CRE analysis of the PBFA-II spectrum indicates that the relatively high intensities from the Al I–IV lines occurred early in the plasma evolution when temperatures were low ($T \lesssim 5$ eV). At these temperatures resonant self-absorption is negligible because of the lack of vacancies in the $2p$ shell. The intensities from the Al V–Al IX satellites were significantly reduced by self-absorption effects. Our analysis suggests that the maximum temperatures attained in the outer (observable) part of the target plasma were about 30 to 45 eV.

Hydrodynamic and PIC simulations of the PBFA-II experiment suggest that carbon ions in the beam played an important role in heating the outer skin of the target plasma. Although carbon-induced ionizations cannot at this point be absolutely ruled out as contributing to the observed K_α spectrum, both the lack of any evidence for multiple ionization events [8] and the low particle flux for the carbon contaminants suggest the spectrum is primarily produced as a result of proton-impact ionization.

K_α emission spectroscopy may offer important opportunities for diagnosing both plasma and beam properties in future light ion beam experiments. Time-resolved spectra using relatively thin ($\sim$ 100–1000 Å) tracer materials could provide valuable temporal and spatial information about target plasma conditions, while reducing problems associated with opacity effects. These aspects will be pursued in future experiments.

Acknowledgements

We wish to thank the entire PBFA II experimental group for their efforts. This work has been supported in part by the U.S. Department of Energy under Contract No. DE-AC04-76DP00789, and by Kernforschungszentrum Karlsruhe (FRG) through Fusion Power Associates. Computing support was provided in part by the National Science Foundation through the San Diego Supercomputer Center.

References

1. A. Hauer, R. D. Cowan, B. Yaakobi, O. Barnouin, and R. Epstein, Phys. Rev. **A 34**, 411 (1986).

2. C. Chenais-Popovics, C. Fievet, J. P. Geindre, J. C. Gauthier, E. Luc-Koenig, J. F. Wyart, H. Pepin, and M. Chaker, Phys. Rev. **A 40**, 3194 (1989).

3. J. Bruneau, C. Chenais-Popovics, D. Desenne, J.-C. Gauthier, J.-P. Geindre, M. Klapisch, J.-P. Le Breton, M. Louis-Jacquet, D. Naccache, and J.-P. Perrine, Phys. Rev. Lett. **65**, 1435 (1990).

4. S. J. Davidson, J. M. Foster, C. C. Smith, K. A. Warburton, and S. J. Rose, Appl. Phys. Lett. **52**, 847 (1988).

5. D. M. O'Neil, C. L. S. Lewis, D. Neely, and S. J. Davidson, Phys. Rev. **A 44**, 2641 (1991).

6. J. Abdallah, Jr., R. E. H. Clark, and J. M. Peek, Phys. Rev. **A 44**, 4072 (1991).

7. T. S. Perry, S. J. Davidson, F. J. D. Serduke, D. R. Bach, C. C. Smith, J. M. Foster, R. J. Doyas, R. A. Ward, C. A. Iglesias, F. J. Rogers, J. Abdallah, Jr., R. E. Stewart, J. D. Kilkenny, and R. W. Lee, Phys. Rev. Lett. **67**, 3784 (1991).

8. J. Bailey, A. L. Carlson, G. Chandler, M. S. Derzon, R. J. Dukart, B. A. Hammel, D. J. Johnson, T. R. Lockner, J. Maenchen, E. J. McGuire, T. A. Mehlhorn, W. E. Nelson, L. E. Ruggles, W. A. Stygar, and D. F. Wenger, Lasers and Particle Beams **8**, 555 (1990).

9. E. Nardi, and Z. Zinamon, J. Appl. Phys. **52**, 7075 (1981).

10. J. P. Van Devender and D. L. Cook, Science **232**, 831 (1986).

11. D. L. Cook et al., Plasma Phys. and Controlled Fusion **28**, 1921 (1986).

12. D. J. Johnson et al., *Proc. of the 7th IEEE Pulsed Power Conf.*, Monterey, CA, 944 (1989).

13. R. J. Leeper et al., *Proc. of Workshop on Diag. for Cont. Fusion Exp.* (ed. by P. E. Stott, D. K. Akulina, G. Gorini, and E. Sindoni, Societa Italiana di Fisica Press, Bologna, Italy, 1991), p. 1051.

14. B. L. Henke, H. T. Yamada, and T. J. Tanaka, Rev. Sci. Instrum. **54**, 1311 (1983).

15. B. A. Hammel and L. E. Ruggles, Rev. Sci. Instrum. **60**, 2861 (1989).

16. B. A. Hammel, D. W. Phillion, and L. E. Ruggles, Rev. Sci. Instrum. **61**, 1920 (1990).

17. X-ray Optics Inc., Jacksonville, Fl.

18. B. L. Henke et al., J. Opt. Soc. Am. B **3**, 1540 (1986).

19. P. D. Rockett et al., Appl. Opt. **24**, 2536 (1985).

20. L. L. House, Astrophys. J. Suppl. **18**, 21 (1969).

21. B. L. Henke, private communication.

22. J. J. MacFarlane and P. Wang, Laser and Particle Beams, in press (1992). More details on CRE model are provided in University of Wisconsin Fusion Technology Institute Reports UWFDM-822 (1990), UWFDM-847 (1991), and UWFDM-873 (1992).

23. J. P. Apruzese, J. David, D. Duston, and K. G. Whitney, J.Q.S.R.T. **23**, 479 (1980).

24. J. J. MacFarlane, Astron. Astrophys., in press (1992).

25. H. Griem, Phys. Rev. **165**, 258 (1968).

26. D. Duston, R. W. Clark, J. Davis, and J. P. Apruzese, Phys. Rev. A **27**, 1441 (1983).

27. C. F. Fischer, Comput. Phys. Commun. **14**, 145 (1978).

28. R. Glass and A. Hibbert, Comput. Phys. Commun. **16**, 19 (1978).

29. P. Wang, J. J. MacFarlane, and G. A. Moses, submitted to Phys. Rev. A (1992).

30. A. Burgess and M. C. Chidichchimo, Mon. Not. R. Astr. Soc. **203**, 1269 (1983).

31. M. J. Seaton, in *Atomic and Molecular Processes*, p. 374, edited by D. R. Bates (Academic Press, New York, 1962).

32. I. I. Sobelman, L. A. Vainshtein, and E. A. Yukov, *Excitation of Atoms and Broadening of Spectral Lines* (Springer-Verlag, New York, 1981).

33. D. E. Post, R. V. Jensen, C. B. Tarter, W. H. Grasberger, and W. A. Lokke, Atomic Data Nucl. Data Tables **20**, 397 (1977).

34. E. Merzbacher and H. W. Lewis, in *Handbuch der Physik, Vol. 34*, edited by S. Flugge (Springer-Verlag, Berlin, 1958).

35. C. H. Rutledge and R. L. Watson, Atomic Data Nucl. Data Tables **12**, 195 (1973).

36. J. M. Kahn, D. L. Potter, and R. D. Worley, Phys. Rev. A **13**, 1735 (1965)

37. T. A. Mehlhorn, W. E. Nelson,, J. E. Maenchen, W. A. Stygar, C. L. Ruiz, T. R. Lockner, and D. J. Johnson, Rev. Sci. Instrum. **59**, 1709 (1988).

38. T. A. Mehlhorn, J. Appl. Phys. **52**, 6522 (1981).

39. L. A. Woltz and C. F. Hooper, Jr., Phys. Rev. A **38**, 4766 (1988).

40. R. C. Mancini, D. P. Kilcrease, L. A. Woltz and C. F. Hooper, Jr., Comp. Phys. Comm. **63**, 314 (1991).

41. R. D. Cowan, *The Theory of Atomic Structure and Spectra*, University of California Press (Berkeley, 1981).

42. L. A. Woltz, V. L. Jacobs, C. F. Hooper, Jr. and R. C. Mancini, Phys. Rev. A **44**, 1281 (1991).